Journal of Nuclear Materials 398 (2010) 220–226

Contents lists available at ScienceDirect

Journal of Nuclear Materials

journal homepage: www.elsevier.com/locate/jnucmat

Temperature and particle size effects on flow localization of 9–12%Cr ferritic/martensitic steel by *in situ* X-ray diffraction and small angle scattering

Xiao Pan [a], Xianglin Wu [a], Xiang Chen [a], Kun Mo [a], Jonathon Almer [b], Dean R. Haeffner [b], James F. Stubbins [a,*]

[a] Department of Nuclear, Plasma and Radiological Engineering, University of Illinois at Urbana-Champaign, Urbana, IL 61801, USA
[b] Advanced Photon Source, Argonne National Laboratory, Argonne, IL 60439, USA

A B S T R A C T

Radiation-induced defect structures are known to elevate material yield strength and reduce material ductility so that small strains induce plastic instability. This process is commonly known as *flow localization*. Recent research indicates that the flow localization in face-centered cubic (FCC) materials is controlled by *critical stress*, the true stress at the onset of necking. Critical stress is found to be independent of irradiation dose, but have strong temperature dependence. Here simplified 9–12% ferritic/martinsetic steels are examined using X-ray diffraction and small angle scattering under *in situ* tensile deformation, in order to elucidate the controlling mechanisms and temperature dependence of critical stress. It is found that the critical stress for the onset of necking is linearly correlated with critical interfacial strength, which in turn determines the void nucleation. The effects of temperature and particle size on critical stress are correspondingly determined by how temperature and particle size influence the critical interfacial strength.

1. Introduction

The issue of materials embrittlement during irradiation exposure continues to be a topic of major concern for advanced nuclear systems. The damage microstructure developed during irradiation restricts dislocation flow so that the plastic deformation is confined to very small volumes or regions of materials under tensile loads [1–3]. These effects reduce the ability of materials to distribute plastic flow uniformly during deformation and limit materials useful life in radiation environments. Recent work [4–6] indicates that the tendency for embrittlement in face-centered cubic (FCC) materials is not directly controlled by a change of yield strength, but rather that fracture is controlled by a critical stress. Results further show that the critical stress is independent of radiation dose level but correlated with material initial condition [4], and has a strong temperature dependence [6]. Besides 316L SS, other FCC materials, body-centered cubic (BCC) and hexagonal closed packed (HCP) materials, such as Cu [4], 304 SS, Ni, Au [7], A533B, and Zircaloy-4 alloy [8], etc. also express this behavior. Taken together, it appears that the critical stress is an intrinsic material property controlling material fracture, and it is thus important to understand the controlling mechanism, or mechanisms, of critical stress.

It is believed that critical stress is associated with critical interfacial strength between particle and matrix, which determines the void nucleation. Voids can initiate by decohesion at the particle–matrix interface and/or by fracture of the inclusion themselves [9]. For the particle-matrix interface decohesion case, voids start to nucleate once the maximum stress at the interface between particle and matrix is larger than the critical interfacial strength. Several initiation models have been built to predict critical interfacial strength based on dislocation interaction and continuum calculations [10,11]. However, all of these models are limited because they were derived from post-deformation microstructural characterization, which contains no information about the dynamic process involved in the evolution of failure. High-energy X-ray diffraction and small angle X-ray scattering methods provide a unique bulk probe of the lattice strains within both the particle and matrix phases for various crystallographic orientations and void evolution, and furthermore can be performed during *in situ* tensile testing [12]. The stress between particle and matrix can be calculated directly based on matrix/particle elastic mismatch, matrix plasticity, interface decohesion and even particle fracture. Thus the correlation between critical interfacial strength for void nucleation and critical stress for onset of necking can be investigated thoroughly.

2. Experimental procedure

Four types of simplified ferritic/martensitic model alloys were selected here. These model alloys are based on the Fe–Cr–C composition produced by Carpenter Technology Corporation. The nominal chemical compositions of four types of model alloys are Fe–9%Cr–0.1%C, Fe–9%Cr–0.5%C, Fe–12%Cr–0.2%C, and Fe–12%Cr–0.5%C,

* Corresponding author. Tel.: +1 217 3336474; fax: +1 217 3332906.
E-mail address: jstubbin@illinois.edu (J.F. Stubbins).

0022-3115/$ - see front matter © 2010 Elsevier B.V. All rights reserved.
doi:10.1016/j.jnucmat.2009.10.035

respectively. The concentrations of Cr in model alloys are very similar with Modified 9Cr–1Mo (T91) and HT9, which are the promising candidates for advanced reactor systems including the fusion reactor (ITER) and accelerator-based neutron systems (SNS) due to their high performance at elevated temperature, low thermal stress and low liquid metal corrosion rates [13,14]. Thus, the results from this work will also offer valuable insights into these alloys. The ingots were hot forged to obtain small slabs (600 × 200 × 40 mm). After hot forging, the alloys were re-austenitisized at 980 °C for 30 min and cooled down in air to room temperature, and then tempered at 720 °C for 4 days, 8 days and 16 days and cooled in the air. The different tempering times provided spheroidized carbides with three distinct particle sizes and size distributions according to the TTT curve of chromium steel [15]. After heat treatment, the plates were cut to make tensile specimens (flat SS-3 type) with nominal gage length of 7.62 mm, width of 1.52 mm and thickness of 0.76 mm.

High-energy X-ray diffraction and small angle scattering measurements were carried out at the 1-ID beamline of the Advanced Photon Source (APS) in Argonne National Laboratory. *In situ* uniaxial tensile tests were performed on a MTS closed-loop servo-hydraulic test frame under displacement control. All tensile tests were conducted at a crosshead speed of 0.005 mm/s, corresponding to an initial specimen strain rate of 10^{-3}/s. The general setup for these experiments is shown in Fig. 1. The test for each sample included two stages, continuous test and interrupted test. In the continuous test, the sample was continuously stretched up to some level of strain but before ultimate tensile strength (UTS), and the position of X-ray measurement was fixed. The diffraction measurements were conducted continuously with a monochromatic 81 keV (λ = 0.015 nm) X-ray beam every 20 s, with an incident beamsize of 100 × 100 μm^2. In the interrupted test, the test stopped in some strain levels, and diffraction measurements were carried out at 7–13 different locations of sample along the (vertical) loading direction. Thus the stress/strain spatial distribution could be observed, especially after necking when deformation is highly non-uniform. Complete Debye–Scherrer diffraction rings from the α-Fe matrix and the carbide precipitates present in the diffraction volume were recorded using an area detector (GE angio type). An ion chamber and a PIN diode (p-type, intrinsic, n-type diode) embedded within the beam stop were used to measure the initial and transmitted beam intensity, respectively. The sample-to-camera distance was 1.369 m.

In order to investigate the temperature dependence of critical stress, specimens from Fe–9%Cr–0.5%C alloy were tested at room temperature, 100 °C and 400 °C for all three different heat treatment conditions. For high temperature testing, heating was achieved via infrared bulbs, and X-ray measurements did not commence until the temperature was found to be stable within ±1 °C, which typically took 10 min.

High X-ray energies produce forward-scattered Debye cones (wide angle scattering or diffraction, WAXS) from a given phase and reflection, and these form rings on the area detector. The lattice spacings probed by WAXS are typically in the 1–10 A range. In addition, small angle scattering (SAXS), in the vicinity of direct beam, is produced by inhomogeneities in electron density over a larger size range (typically 10–1000 nm), which in the present case are primarily voids. The high-energy scattered X-rays from both SAXS and WAXS, measured with the area detector, correspond to a 2-D slice of sample orientation, which is to a good approximation perpendicular to the incident beam direction.

Properties measured by WAXS include both degree of texture and internal strain. In the case of random orientation, the intensity of each diffraction ring is uniform. Otherwise, the variation of intensity around azimuthal direction corresponds to the presence of texture. The elastic strain for each phase and reflection can be evaluated from changes in d-spacing as a function of orientation. In the case of uniaxial deformation, a given phase is generally under deviatoric (directional) strains, which produces elliptical diffraction rings, and this strain can be quantified by fitting the radial peak profile as a function of azimuthal angle. More details of the analysis procedure can be found in Young et al. [16].

3. Results

3.1. Steel microstructure and tensile results

The microstructures of undeformed samples for each model alloy were evaluated by SEM as shown in Fig. 2. The samples were etched by Vilella's Reagent (3 parts glycerol, 1 part nitric acid and 2 parts hydrochloric acid) so that the ferrite and carbide structure can be easily distinguished. It is clear that systems are very simple, with only carbide and ferrite phases present. The particle volume fraction changes significantly for these four types of model alloys, due to differing carbon contents. The effect of heat treatment on the particles is similar for all alloys. The average particle size increases with tempering time, but there is not much difference especially after long time tempering as shown in Fig. 3.

Fig. 4 shows the macroscopic deformation results of Fe–9%Cr–0.5%C-16d tested at room temperature, 100 °C and 400 °C from X-ray *in situ* tensile testing. In the continuous measurement mode, X-ray measurements were done simultaneous to the deformation so that the stress increases continuously with strain. Once the testing mode was switched to the y-scanning measurements mode, the testing was conducted stepwise. During the holding time, the external stress is reduced due to stress relaxation so that there is a stress drop for the first y-scan measurements. This phenomenon was also reported in neutron *in situ* measurements previously, where even longer holding times were conducted [17].

3.2. Void evolution

The damage evolution during the *in situ* tensile test was measured by small angle X-ray scattering (SAXS). At each measured strain level, the damage information can be plotted by relationship

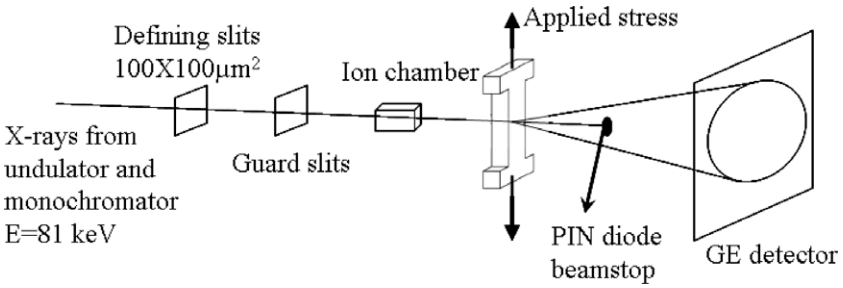

Fig. 1. Schematic of experimental diffraction setup.

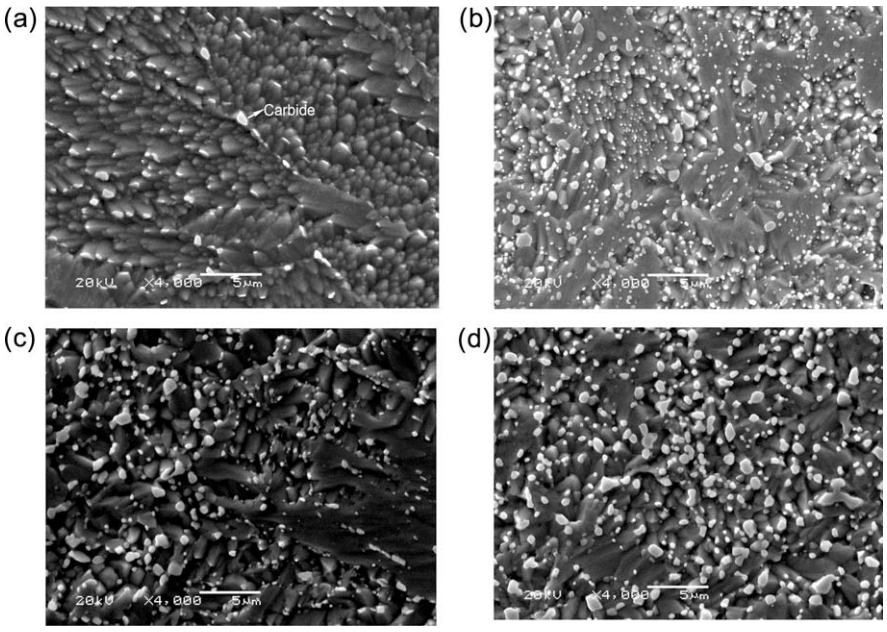

Fig. 2. SEM micrographs of model alloys: (a) Fe–9%Cr–0.1%C-4d, (b) Fe–9%Cr–0.5%C-4d, (c) Fe–12%Cr–0.2%C-4d, and (d) Fe–12%Cr–0.5%C-4d, carbide phase is indicated in (a).

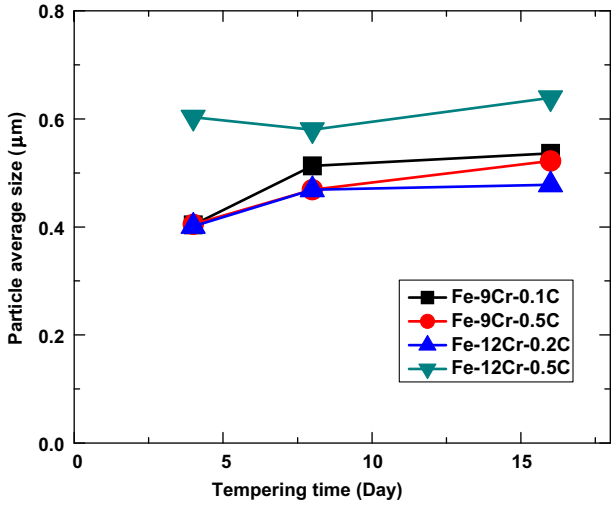

Fig. 3. Average particle size of four model alloys vs. tempering time.

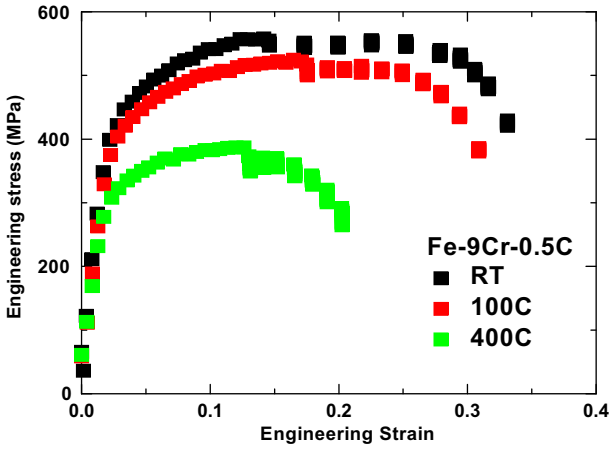

Fig. 4. Tensile behaviors of Fe–9%Cr–0.5%C-16d tested at room temperature, 100 °C and 400 °C by X-ray *in situ* tensile test.

between scattering intensity and Q-vector. Fig. 5 shows the calibrated scattering intensity vs. Q-vector for Fe–9%Cr–0.5%C-16d at different strain levels tested at room temperature. Each line is corresponded to each measured point during the test as shown in Fig. 4. After reaching UTS, only the point closed to necking center was chosen although there were several measurements along the loading direction. It is clear that the calibrated scattering intensity increases with deformation (or load); however the increase of scattering intensity is slight before UTS. After reaching the UTS, the intensity, jumps up quickly. Although other features, such as dislocations and second phases, can contribute the scattering intensity, the main contribution is from the presence of voids due to their relatively high contrast factor [18]. The SAXS data was fitted to a Porod slope given by:

$$I = Aq^{-4} + B$$

where I is calibrated scattering intensity, q is Q-vector. A is the Porod constant (scale factor), which can be evaluated by fitting. Since

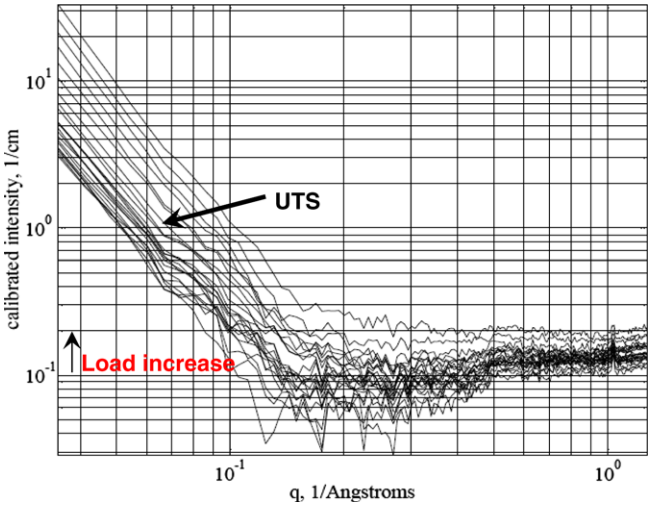

Fig. 5. SAXS profiles of Fe–9%Cr–0.5%C-16d tested at room temperature.

voids mainly contribute to the increasing scattering intensity, increases in *A* are attributed to increases in void fraction. Fig. 6 shows *A* values versus applied strain for Fe–9%Cr–0.5%C-16d alloy tested at room temperature (Black line with rectangular shape stands for the necking point during the test, other color lines stands for several measuring points at various distances away from the necking point along the loading direction). It is clear that there are no measurable voids nucleated in the elastic region. Once the deformation passes the yield point, a small number of voids start to nucleate. The voids nucleate continuously as the strain increases. It is believed that this continuous void nucleation is related to the complex local conditions around the particles, which involves the particle size, particle shape, particle distribution. Thus the critical nucleation condition for different particles is achieved at a variety of strain levels. Babout et al. [19] also discovered the dispersion of damage initiation in the Al-ZS system by X-ray tomography. Although certain types of voids start to nucleate upon yielding, the void density up to UTS (22.5%) is still low. The low-void-density tail at small strain is attributed to Type I particles, such as irregular shape particles, extra large particle with defects, and particle clusters [11]. In void nucleation analysis, Type I particles were excluded. The y-scanning measurement before UTS indicates the void distribution is rather uniform along the whole sample. After passing UTS, the void density starts to rise dramatically at or around the necking center. At locations far away from the necking center, the void density keeps nearly the same level as observed at UTS. From this observation, we posit that the UTS is the critical point for void nucleation. Detailed SEM analysis further shows that the main voids are associated with Type I particles before UTS, and voids start to nucleate around larger particles first in a regular particle distribution, and then extend to small particles after passing UTS.

3.3. Lattice strain evolution

Fig. 7 shows the lattice strain response of ferrite and carbide of Fe–9%Cr–0.5%C-16d tested at room temperature. (2 2 0) and (4 4 0) Reflections are used for matrix and particle, respectively. The response of lattice plane strain in ferrite can be divided into three stages, namely the elastic (A), grain to grain yield (B), and stage III (C). In the elastic region, the lattice strains along the loading (axial) direction increase linearly with increasing of applied stress. From this linear relationship, elastic constants can be calculated including Young's modulus and Poisson ratio. During the yield region, axial lattice strain shows the compressive shifts, which are correlated with load partition between matrix and particle. Once plastic deformation develops equally through all of the grains, the yield process stops and material enters the plastic deformation stage where dislocation accumulation takes place. In the elastic region, the matrix and particle show near-zero mismatch. The slopes of the elastic response on both matrix and carbide are 234 GPa and 240 GPa, respectively, which is in good agreement with the macroscopically determined Young's modulus. The similarity of the elastic stiffness between the matrix and reinforcement phases has been reported by other researchers [16].

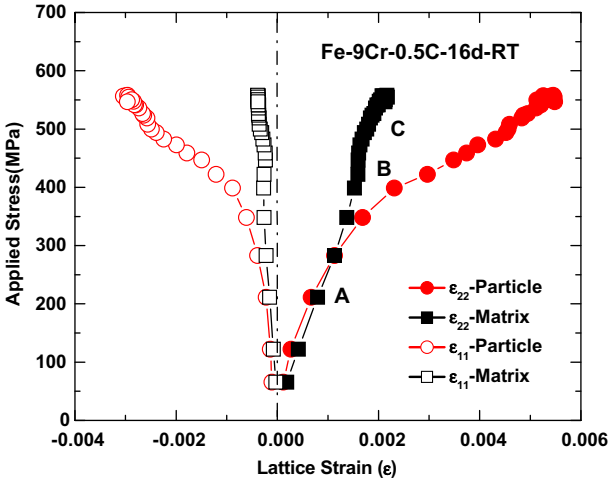

Fig. 7. Applied stress vs. lattice strain for Fe–9%Cr–0.5%C-16d.

Fig. 8 shows the axial lattice strain vs. applied strain for matrix and particle of Fe–9%Cr–0.5%C-16d tested at room temperature, 100 °C and 400 °C. It is clear that the axial lattice strain of matrix and particle overlap within the elastic region. With increasing applied strain, the matrix starts to yield and plastic deformation develops in some preferred grains, while the particles are still undergoing elastic deformation. Since there is elastic–plastic mismatch between matrix and particle, the load transfer occurs starting from that point. Temperature has a large effect on the load transfer. With increasing temperatures, the load transfer starts earlier. The strains for load transfer for room temperature, 100 °C and 400 °C are 2.07%, 1.9%, and 1.7%, respectively. The strain for load transfer decreases with increasing temperature, which means the load transfer between matrix and particle is more efficient at high temperature.

Materials deform uniformly up to UTS. Once passing the UTS point, necking starts to occur so that plastic deformation localizes in the necking region. During the necking, the stress develops from a uniaxial to a triaxial state. Since it is difficult to predict the necking region in the flat specimen, the X-ray measurement can miss the necking point if the X-ray beam is measured in a fixed location. Thus y-scanning measurement was applied for the second testing step. Fig. 8 also shows the lattice strain from the y-scanning measurements with respect to applied strain. A couple of points before UTS are also included. Before UTS, the lattice strain in the matrix phase is rather uniform, which indicates uniform deformation within the gage section prior to UTS. Past the UTS point, the extent of the scatter increases. Depending on position, the lattice strains continue to increase until fracture, continue to increase prior to decreasing or start to drop right away. At 400 °C, there is no position where lattice strain increases continuously. It is possible that the precise necking point was not be evaluated in this case. The position dependence of the lattice strain matches the deformation localization after necking. When necking occurs, the deformation concentrates in the necking region, especially at the necking point,

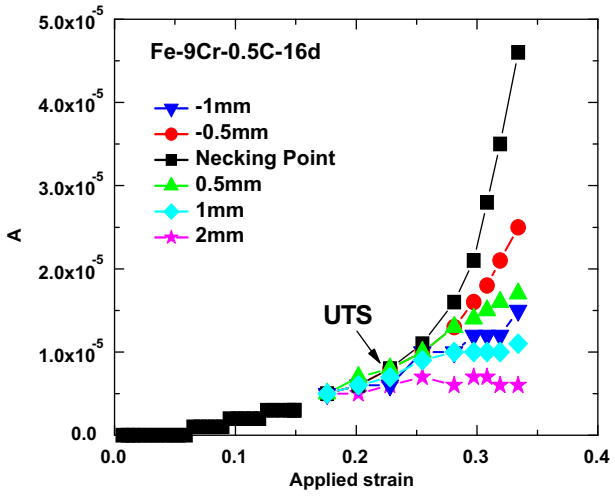

Fig. 6. Porod A vs. applied strain for Fe–9%Cr–0.5%C-16d tested at room temperature.

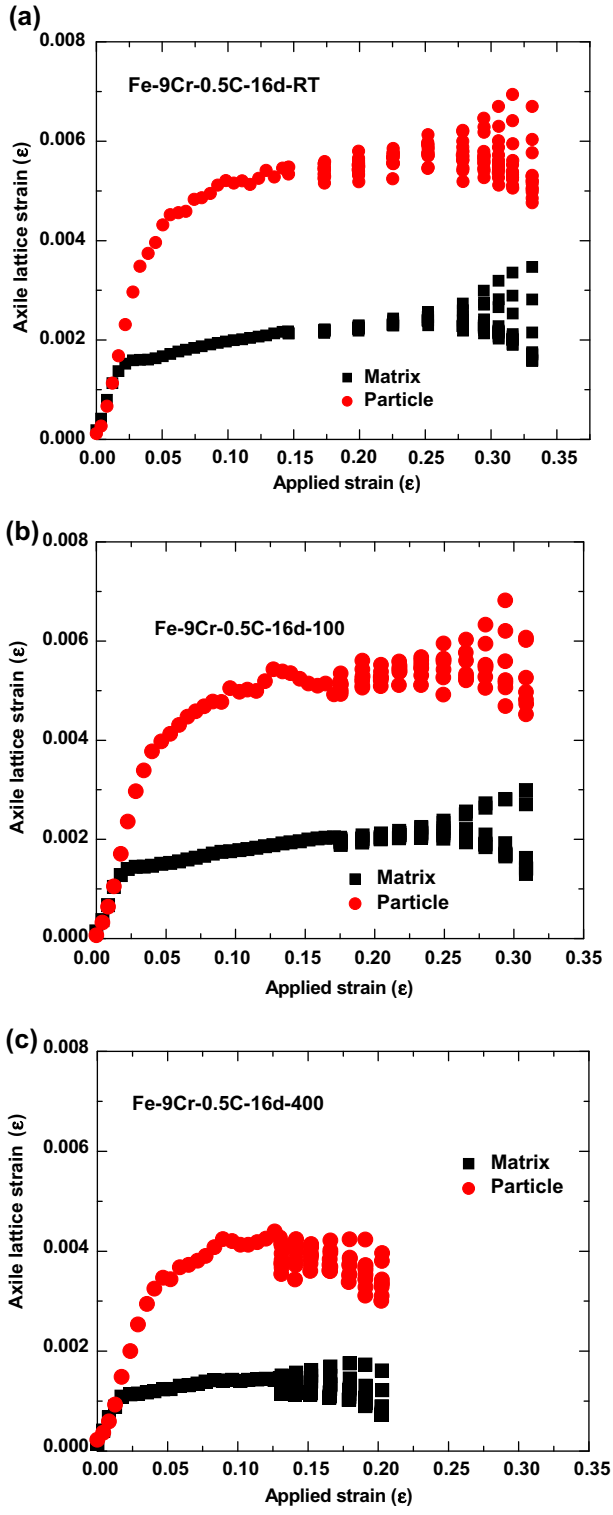

Fig. 8. Axial lattice strain vs. applied strain for matrix and particle of Fe–9%Cr–0.5%C-16d tested at (a) room temperature, (b) 100 °C, and (c)400 °C.

while other parts of material far away from the necking point starts to relax.

3.4. Stress analysis

Once the axial (ε_{22}) and transverse (ε_{11}) lattice strain of an $h\,k\,l$ peak from a given diffraction peak are measured from peak shifts, the internal stress on the particle can be analyzed by [16]:

$$\sigma_{22} = \frac{E}{1+\nu}\varepsilon_{22} + \frac{\nu E}{(1+\nu)(1-2\nu)}(\varepsilon_{22}+\varepsilon_{11}+\varepsilon_{33})$$

$$\sigma_{11} = \sigma_{33} = \frac{E}{1+\nu}\varepsilon_{11} + \frac{\nu E}{(1+\nu)(1-2\nu)}(\varepsilon_{11}+\varepsilon_{22}+\varepsilon_{33})$$

where σ_{22} is axial principle stress, σ_{11} and σ_{33} are transverse principle stress. E_{hkl} and ν_{hkl} from experiment are used for each ($h\,k\,l$) reflection. During the tensile test, the particles always maintain elastic deformation. High-energy X-ray diffraction can directly measure the elastic strain on the particles. Through strain and stress analysis on the particle, the stress evolution during the tensile test can be evaluated. The internal stress behavior shows similar response as lattice strain. The internal stress increases with increasing of applied strain uniformly up to UTS. After passing UTS, the stress shows scattered behavior. The stress on the particles at or close to the necking point still keeps increasing. While the stress on other particles away from the necking point keeps increasing for some extents of strain and then drops. It is believed that secondary dislocations are developed in the matrix during the necking and these dislocation keeps pushing up the stress on the particles [20]. Since the deformation is localized in the necking point, other parts of sample starts to relax once passing the UTS, which make the stress level on the particle decreases.

Results from small angle X-ray scattering indicate that voids start to nucleate around the large particle for each specific size distribution at UTS. Thus the internal stress on the particle right at UTS is the critical stress for void nucleation of large particle, or critical interfacial strength between matrix and particle. Although the internal strain measured from X-ray diffraction is the average elastic strain of all particles in a particular sample volume, it can provide valuable indication of the critical interfacial strength between particle and matrix.

4. Discussion

4.1. Temperature effect

According to dislocation theory, dislocations become more mobile so that the stress relaxation is easier as the test temperature increases. Furthermore, from the load partitioning measured here, load transfer starts earlier and is more effective with increasing temperature. Both stress relaxation and load transfer mechanisms should lead to increased uniformity in material deformation. However, uniform elongation is found to decrease, and failure rate increase, with increasing temperature. Fig. 9 shows the temperature effect on critical interfacial strength of Fe–9%Cr–0.5%C alloys. It is clear that critical interfacial strength decreases with increasing temperature. By applying the temperature dependence of critical interfacial strength, the ductility loss at elevated temperature can be explained. Because the critical interfacial strength is much lower at high temperature, the barrier for void nucleation is lower. Once the void nucleates, high temperatures promote void growth and coalescence, which increases failure rate. Zhao et al. [21] investigated the fracture behavior of 2014/AlO system and found that the void nucleation mechanism switches from particle fracture at low temperature to interfacial debonding at elevated temperature. Their observation strongly supports the temperature dependence of the critical interfacial strength. At low temperature, good bonding between matrix and reinforcing particle leads to void initiation in particle cracking mode, while the interfacial debonding is dominant at high temperature due to the degradation of critical interfacial strength.

4.2. Particle size effect

The effects of particle morphology, including size, shape and volume fraction, on the damage process have been carried out widely in

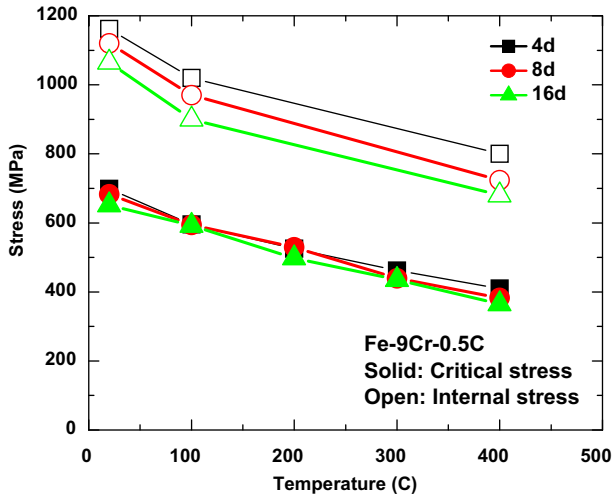

Fig. 9. Internal stress and critical stress of Fe–9%Cr–0.5%C alloys tested at room temperature, 100 °C and 400 °C.

experiment [22] and FEM modeling [23]. The ductile fracture process starts from large particle and ends with the linkage between voids around the large particle. As shown in Fig. 9, the critical interfacial strength of Fe–9%Cr–0.5%C alloys for three different heat treatments decreases with increasing average particle size. In addition, Fig. 10 shows the maximum normal stress around the particle versus the true strain of Fe–9%Cr–0.5%C-16d tested at room temperature. As the fracture process continues after passing UTS, the maximum normal stress around the particle increases up to 1500 MPa. From the void nucleation process, void nucleation starts from large particle, and then extends to small particle with further deformation. The increase of maximum normal stress around particle just matches the sequence of void nucleation, i.e. from large particle to small particle. Toda et al. [24] also found values of the maximum principle stress for $CuAl_2$ and Al_2CuMg particles with diameters between 5 and 8 μm is 710 MPa, while for larger particle size, between 14 and 18 μm, the maximum principle stress is around 540 MPa. Shabrov and Needleman [23] used finite element model to analyze the particle size effect on void nucleation and found similar results as experiment**.** In a word, the interfacial strength has size dependence, i.e. increasing with decreasing of particle size.

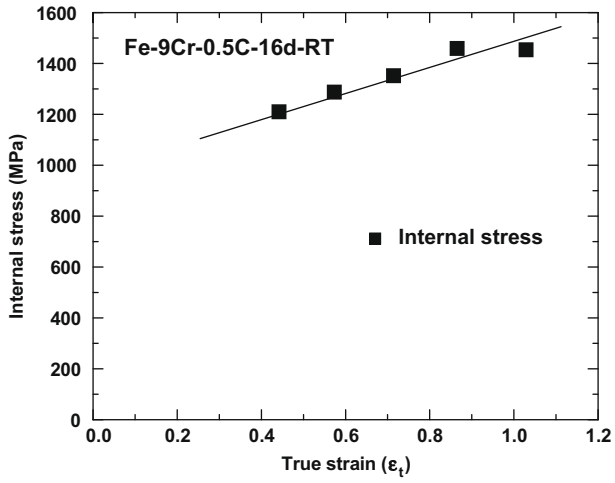

Fig. 10. Maximum internal stress on particle vs. true strain.

4.3. Interfacial bonding

Both temperature and particle size effects are eventually related with the interfacial bonding between particle and matrix. Elevated temperature and pre-existed defects around large particle might weaken the interfacial bonding, i.e. lower the critical interfacial strength. The interfacial cohesion bond is material property and depends on several factors, such as the composition of matrix and particle, impurity, and particle crystal orientation. Prangnell et al. [25] investigated the fracture of two MMC systems, 6061 aluminum matrix composite reinforced with alumina, and aluminum 9 wt.% Si alloy reinforced with silicon carbide particles. They discovered that the interface bond in SiC reinforced material is far stronger leading to particle cracking, while there is a reaction layer between alumina and matrix to weaken the interfacial bonding, which results in interfacial debonding. One of this work's purposes is to investigate the interfacial bonding effect on the void nucleation by changing the composition. Fig. 11 shows the critical interfacial strength of model alloys tested at room temperature. It is interesting to notice that the interfacial strength separates into two regions. Although there is a big difference of chemical composition among Fe–9%Cr–0.1%C, Fe–12%Cr–0.2%C and Fe–12%Cr–0.5%C alloys, their critical interfacial strengths are similar and around 1380 MPa at room temperature. The critical interfacial strength of Fe–9%Cr–0.5%C alloy is about 1160 MPa at room temperature, which is much lower than those of other three alloys. X-ray diffraction distinguishes different carbide crystal structures in these four alloy systems. In Fe–9%Cr–0.5%C alloy, the main carbide is HCP structure, M_7C_3, while cubic $M_{23}C_6$ particles are dominant in Fe–9%Cr–0.1%C, Fe–12%Cr–0.2%C and Fe–12%Cr–0.5%C alloys. Previous research has already shown the orientation relationship between $M_{23}C_6$ particle and ferrite is Kurdjumov-Sachs type, while a different orientation relationship exists for M_7C_3 carbide with respect to ferrite [26]. Although the chemical compositions are different among Fe–9%Cr–0.1%C, Fe–12%Cr–0.2%C and Fe–12%Cr–0.5%C alloys, they have similar interfacial strength due to the same particle crystal structure and orientation relationship with ferrite. Thus the critical interfacial strength is mainly determined by the particle crystal structure. In addition, it is noticed that critical interfacial strength is independent of particle volume fraction. Fe–12%Cr–0.2%C and Fe–12%Cr–0.5%C alloys has same critical strengthen with different particle volume fraction.

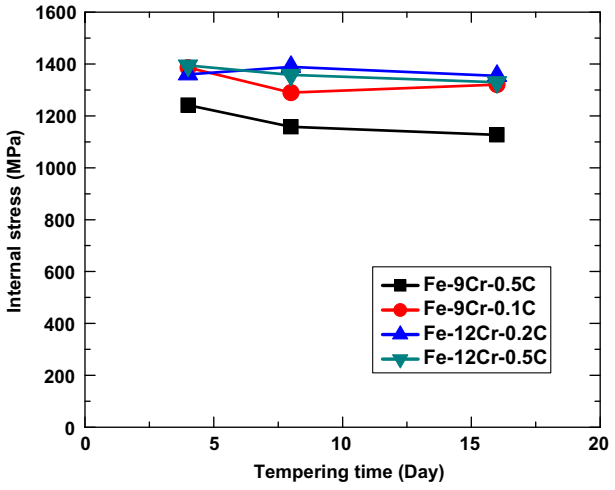

Fig. 11. Critical interfacial strength vs. tempering time for four types of model alloys tested at room temperature.

4.4. Controlling mechanism of critical stress

Fig. 9 shows both the critical stress and critical interfacial strength as a function of temperature. It is obvious that the critical stress is directly correlated with critical interfacial stress, and this can be expressed by the linear relationship:

$$\sigma_{interfacial} \approx (1.5{-}1.8)\sigma_{critical}$$

This relationship indicates that the critical stress for the onset of necking, on the macroscopic level, is controlled by the critical interfacial stress, on the microscopic level. Qiu et al. [27] reported that cold work decreases the critical interfacial strength of X-65 steel, which is consistent with our previous result that the cold work decreases the critical stress for onset of necking for 316L stainless steel [6]. This further indicates that the critical interfacial strength controls the critical stress for onset of necking. The effects of temperature and particle size on critical stress are correspondingly determined by how temperature and particle size influence critical interfacial strength, which is consistent with experimental observations.

5. Conclusions

In situ tensile test of model alloys were performed at different temperatures in APS at Argonne National Laboratory. The lattice strain evolution was measured using wide angle scattering, while void nucleation was tracked using small angle scattering. The controlling mechanism of critical stress for onset of necking and temperature dependence of critical stress were systematically evaluated, in addition to the role of secondary particle size. The following conclusions could be drawn:

1. UTS is a critical and starting point for void nucleation. Void nucleation occurs first around large particles in each particle distribution after passing UTS.
2. Critical interfacial strength has strong temperature dependence. Critical interfacial strength decreases with increasing temperature.
3. The microstructure of secondary particles has significant effects on the critical interfacial strength. The critical interfacial strength decreases with increasing particle size, and is strongly correlated with particle crystal structure. On the other hand, the particle volume fraction has a negligible effect on critical interfacial strength, over the range of VF studied here.
4. The critical stress for the onset of necking is linearly correlated with critical interfacial strength. The effects of temperature and particle size on critical stress are correspondingly determined by how temperature and particle size influence critical interfacial strength. The critical stress is a material property only depending on initial conditions, since critical interfacial strength is a material property.

Acknowledgements

The work was supported by the US Department of Energy under grants DE-FC07-051D14665, DE-FG07-02D14337 and (APS) under DE-AC02-06CH11357.

References

[1] K. Kitajima, H. Abe, Y. Aono, E. Kuramoto, S. Takamura, J. Nucl. Mater. 108–109 (1982) 436–441.
[2] K. Farrell, T.S. Byun, J. Nucl. Mater. 329–333 (2004) 998–1002.
[3] S.A. Maloy, M.R. James, G. Willcutt, W.F. Sommer, M. Sokolov, L.L. Snead, M.L. Hamilton, F.A. Garner, J. Nucl. Mater. 296 (2001) 119–128.
[4] X. Pan, X. Wu, M. Li, J.F. Stubbins, J. Nucl. Mater. 329–333 (2004) 1088–1092.
[5] X. Wu, X. Pan, M. Li, J.F. Stubbins, Trans. Am. Nucl. Soc. 91 (2004) 918–919.
[6] X. Wu, X. Pan, M. Li, J.F. Stubbins, J. Nucl. Mater. 343 (2005) 302–307.
[7] X. Wu, X. Pan, M. Li, J.F. Stubbins, J. ASTM Int. 3 (2006) 185–198.
[8] T.S. Byun, J. Nucl. Mater. 361 (2007) 239.
[9] S.H. Goods, L.M. Brown, Acta Metall. 27 (1979) 1–15.
[10] A.S. Argon, J. Im, Metall. Trans. 6A (1973) 839.
[11] D. Kwon, R.J. Asaro, Metall. Trans. 21A (1990) 117.
[12] J.D. Almer, S.R. Stock, J. Struct. Biol. 152 (2005) 14.
[13] J. Henry, X. Averty, Y. Dai, P. Lamagnere, J.P. Pizzanelli, J.J. Espinas, P. Wident, J. Nucl. Mater. 318 (2003) 215–227.
[14] R.L. Klueh, D.S. Gelles, S. Jitsukawa, A. Kimura, G.R. Odette, B. van der Schaaf, M. Victoria, J. Nucl. Mater. 307–311 (2002) 455–465.
[15] J.V. Bee, R.W.K. Honeycombe, Metall. Trans. 9A (1978) 587.
[16] M.L. Young, J.D. Almer, M.R. Daymond, D.R. Haeffner, D.C. Dunand, Acta Mater. 55 (2007) 1999–2011.
[17] E.C. Oliver, M.R. Daymond, P.J. Withers, Acta Mater. 52 (2004) 1937–1951.
[18] G.G. Long, L.E. Levine, R.J. Fields, Mater. Sci. Eng. A. 309–310 (2001) 28.
[19] L. Babout, E. Maire, R. Fougeres, Acta Mater. 52 (2004) 2475.
[20] T.S. Byun, K. Farrell, Acta Mater. 52 (2004) 1597–1608.
[21] D. Zhao, F.R. Tuler, D.J. Lloyd, Acta Metall. Mater. 42 (1994) 2525–2533.
[22] I. Sabirov, O. Kolednik, Scripta Mater. 53 (2005) 1373–1378.
[23] M.N. Shabrov, A. Needleman, Model. Simul. Mater. Sci. Eng. 10 (2002) 163–183.
[24] H. Toda, T. Kobayashi, A. Takahashi, Alum. Trans. 1 (1999) 109.
[25] P.B. Prangnell, S.J. Barnes, S.M. Roberts, P.J. Withers, Mater. Sci. Eng. A 220 (1996) 41–56.
[26] P.R. Howell, J.V. Bee, P.W.K. Honeycombe, Metall. Trans. 10A (1979) 1213.
[27] H. Qiu, H. Mori, M. Enoki, T. Kishi, ISIJ Int. 39 (1999) 358–364.